

Experimental Investigation of the Thermal Decomposition Pathways and Kinetics of TATB by Isotopic Substitution

Batikan Koroglu,*^[a] Jonathan C. Crowhurst,^[a] Evan M. Kahl,^[a] Jason S. Moore,^[a] Ana Racoveanu,^[a] Harris E. Mason,^[a] David G. Weisz,^[a] John G. Reynolds,^[a] and Alan K. Burnham^[a, b]

Abstract: Real-time measurements of the product gases arising from the thermal decomposition of triamino-trinitro benzene (TATB), its deuterated analogue, and plastically bonded TATB (LX-17) are presented in this study. Gas-phase decomposition products are identified by IR absorption spectroscopy. The frequency shifts in rovibrational spectra due to isotopic substitution and the change in rate of formation of decomposition products due to the kinetic-isotope-effect (KIE) help elucidate the decomposition pathways. The formation of H₂O precedes other molecules (e.g., HCN, HNCO) during decomposition. After the concentrations of HCN and HNCO molecules reach a peak, their amounts gradually decrease. The concentrations of the other decomposition products (e.g., NH₃ and CO₂) rapidly rise after an induction period, which is attributed to the presence of autocatalytic reactions. The trends of chemical evo-

lution are similar for all the samples, but their kinetic behaviors are different. This indicates the rates of consistent pathways are changed during thermal decomposition. The kinetics of deuterated TATB decomposition is slower than that of unsubstituted TATB due to the KIE ($k_H/k_D \sim 1.41$). The rate of LX-17 decomposition is slightly lower than unsubstituted TATB ($k_{\text{TATB}}/k_{\text{LX-17}} \sim 1.15$). The KIE is more pronounced during the early stage of decomposition, which is attributed to the first steps of TATB decomposition involving water formation (i.e., H vs D transfer). The KIE slows down the formation of all gases, including those lacking hydrogen (e.g., CO₂). These results suggest the TATB thermal decomposition mechanism might involve a series of pathways rather than a set of independent and parallel reactions.

Keywords: TATB · thermal decomposition · deuterium · isotopic substitution · kinetic-isotope-effect

1 Introduction

1,3,5-Triamino-2,4,6-trinitro benzene (TATB, C₆H₆N₆O₆) is an aromatic molecule with three nitro (NO₂) and three amino (NH₂) functional groups alternating around a benzene ring. TATB is a crystalline solid at room temperature and is an insensitive high explosive (HE) with a remarkably high thermal stability and resilience to impact, friction, and spark. Several studies including decomposition experiments have been conducted to determine the origin and extent of its insensitivity [1–4]. Understanding the decomposition chemistry of TATB is important for developing kinetic models to predict its behavior in abnormal thermal environments (e.g., thermal accident scenarios).

An overall insight into the decomposition chemistry of TATB is gained through the temperature dependent i) heat-release rates measured using differential scanning calorimetry (DSC) [5–8] and ii) weight loss monitored using thermogravimetric analysis (TGA) [9–11]. The results suggest that TATB decomposition involves two consecutive autocatalytic-type reactions. The activation energies (E_a) of thermal decomposition derived from these studies range from 150 kJ/mol (36 kcal/mol) to 250 kJ/mol (60 kcal/mol). Some of these activation energies were used by McGuire and Tarver [12] to model one-dimensional time-to-explosion

(ODTX) experiments. A three-step reaction sequence that describes TATB decomposition was employed to predict the time-to-explosion test results. The model was based on an initial endothermic step producing an unknown solid-phase intermediate, followed by a pair of exothermic steps resulting in an unknown gaseous product. These studies highlighted the need for identifying the specific decomposition products and pathways of generalized reaction schemes.

To gain insights into the first steps of TATB decomposition Sharma et al. conducted degradation experiments prior to full-scale development of an explosion [13–17]. A scanning electron microscope (SEM) was used to locate the remnants of reaction sites induced by heat, ultraviolet photolysis, electron irradiation, shock, or impact. The chemical

[a] B. Koroglu, J. C. Crowhurst, E. M. Kahl, J. S. Moore, A. Racoveanu, H. E. Mason, D. G. Weisz, J. G. Reynolds, A. K. Burnham
Lawrence Livermore National Laboratory, 7000 East Avenue, Livermore, CA, 94550
*e-mail: koroglu1@llnl.gov

[b] A. K. Burnham
M.H. Chew and Associates, 7633 Southfront Road Ste 170, Livermore, CA 94551

 Supporting information for this article is available on the WWW under <https://doi.org/10.1002/prep.202100082>

composition of these sites was analyzed by x-ray photo-electron spectroscopy (XPS), thin layer chromatography (TLC) and chemical ionization/mass spectroscopy. The samples degraded by shock, impact, or electron irradiation contained furazan and furoxan structures, whereas UV photolysis of the sample produced a mono-furazan. The thermally degraded TATB did not contain furoxan (Figure 1b) but showed mono- and di-furazans (Figures 1c, d) and an additional product (Figures 1e) in which two furazan rings were formed and a nitro group was lost and replaced by hydrogen.

The furazan and furoxan structures are more sensitive to impact than TATB [13]. The 50% drop height of amino-dinitro-furoxan is 56 cm, whereas that of TATB is 185 cm. In view of these results, Sharma et al. stated that the reaction of the nitro group and loss of aromaticity that result in mono-furazan formation is common to all stimuli (e.g., heat, ultraviolet photolysis, electron irradiation, shock, or impact) and can be considered as the first endothermic step that sensitizes TATB. Also, the departure of two hydrogen atoms and one oxygen atom from the parent TATB molecule during mono-furazan formation can create a water molecule. They noted that the formation of water might be the first exothermic step releasing the energy required for maintaining the disruptive processes leading to an explosion.

The formation of furazan derivatives of TATB together with other molecules such as water was investigated by Land et al. through *in-situ* measurements of gaseous products at isothermal conditions (e.g. 340 °C) [18]. The temporal evolution of decomposition products was determined via simultaneous thermogravimetric analysis and mass spectrometry measurements ($P < 10^{-6}$ Torr). Several light species were identified (e.g., CO₂, HCN, etc.) in addition to

mono-, di-, and tri-furazan derivatives of TATB, which sequentially formed as a result of stepwise loss of water from the TATB molecule. The concentrations of mono-furazan, H₂O, CO₂, CO and HCN showed an early rise, which was then followed by a later rise of C₂N₂, NO, HNCO, NH₃, di- and tri-furazans. In addition, thermal degradation experiments were performed by heating TATB samples at a rate of 5 °C/min up to 300 °C. The samples were then cooled to room temperature inside the controlled environment of a differential-scanning-calorimeter (DSC) for an *ex-situ* analysis by Atomic Force Microscopy (AFM). The thermally cycled samples exhibited sub-micron size holes (i.e. potential reaction sites) that were similar to the ones observed by Sharma et al. [13]. These results suggest the decomposition of TATB is a non-uniform process catalyzed through reaction sites which might be referred to as 'hot spots'.

The loss of 18 amu from the TATB molecule, attributed to water formation during the early stages of decomposition [19–21], leaves behind a furazan molecule [13, 18]. This process can involve a sequence of chemical events (e.g., unimolecular dissociation, formation of intermediates/radicals), followed by ring closure to form the furazan. The possible mechanisms for the initial steps of TATB decomposition can be gleaned from experimental studies. Sharma et al. reported the decrease of the nitro-nitrogen feature (as opposed to the amine-nitrogen feature) in the XPS spectra of the thermally decomposed TATB [14], suggesting there might be a homolytic C-NO₂ bond scission during TATB decomposition. NO₂ was also reported as a gaseous product in another study that used a Knudsen effusion cell and a mass spectrometer [22]. However, the authors observed several other lighter molecules (e.g., H₂, NH₂, NO) and noted that these species might have formed due to fragmentation of the decomposition products. For that reason, they also used a very low-pressure evaporation cell (Langmuir cell) that was kept in high vacuum (10^{-3} Pa) to prevent collisions between the chemical species. Nearly equal intensity peaks around 144 amu and 114 amu were observed in the mass spectra, suggesting cleavage of the benzene ring as a possible mechanism of TATB decomposition.

Three other possible mechanisms for the initial steps of TATB decomposition were proposed in addition to C-NO₂ bond rupture and ring cleavage. These include bond fissions in C-NH₂, N-O, and N-H. The C-NH₂ bond scission was proposed as the primary step of thermal decomposition by Makashir and Kurian [9]. They recorded the IR spectra of solid TATB samples in KBr matrices at isothermal conditions between 271 °C and 306 °C. The IR band intensities decreased in the order of i) -NH₂ asymmetric stretching (3320 cm^{-1}), ii) NO₂ symmetric stretching (1220 cm^{-1}), and iii) ring stretching vibration (1440 cm^{-1}). This observation suggests the following order of reactivity: amino group > nitro group > ring. They also identified NH₃ as a gaseous product of TATB decomposition, which is consistent with the initial deamination process creating an NH₂ radical and forming NH₃ via H abstraction. Besides C-NH₂

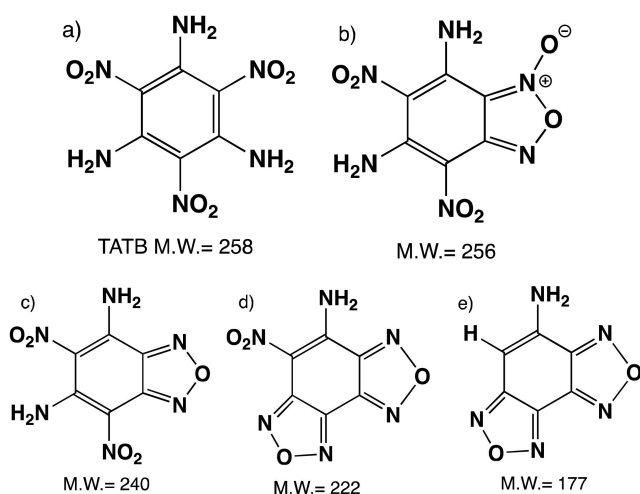


Figure 1. (a) The molecular structure of TATB. (b–d) The products of the molecular breakup of TATB proposed by Sharma et al. [15]: (b) furoxan, (c), (d), and (e) furazans.

bond fission, N–O dissociation was proposed by Ostmark due to the appearance of the $C_6H_6O_5N_6$ molecule in mass spectrometry measurements during shock-induced decomposition of TATB [23].

The last possible mechanism of bond fission during early stages of TATB decomposition is N–H bond rupture. Although direct experimental evidence of this decomposition pathway does not appear to have been reported in the literature, the dynamics of the hydrogen motion as well as the other possible pathways of TATB decomposition were theoretically investigated by Wu and Fried [24]. DFT was used to calculate the energy barriers of the first steps of decomposition: 1) C–NH₂, 2) N–O, 3) N–H, and 4) C–NO₂ single bond scissions, 5) carbon ring cleavage forming $C_3H_2N_3O_4$ and $C_3H_4N_3O_2$ molecules, and 6) intra- or 7) inter-molecular hydrogen transfer processes, where the hydrogen atom of an amino group moves to the nearest oxygen atom of a nitro group and a biradical forms, which then goes through a ring closure and forms a mono-furazan and a water molecule. The energy barriers (i.e., activation energies) were calculated for some of these pathways (e.g., 6 and 7), whereas the energies of reactions were calculated for the others. The reaction energies set the lower bounds for the activation energies of reactions. The TATB decomposition mechanism involving the intra-molecular hydrogen motion was determined to have the lowest activation energy, 47 kcal/mol (197 kJ/mol). Therefore, the reaction channel denoted by 6) above and shown in Figure 2 was reported as the rate-limiting step of TATB decomposition. It was also noted that C–NO₂ bond scission might be a feasible decomposition pathway, because its reaction energy was 63.9 kcal/mol (267 kJ/mol).

Although the initial decomposition reactions of TATB are known to form a water and a furazan molecule, a comprehensive mechanism with specific component reactions, chemical species, and rates describing how furazans evolve and form the lighter gaseous products (e.g., CO₂, HCN, and NH₃) is currently lacking. The use of isotopically labelled TATB samples could help improve our understanding of the decomposition pathways by tracking the changes in the experimental signals due to isotopic substitution. Rogers et al. performed DSC measurements and time-to-explosion tests using deuterated TATB samples to determine the specific functional groups involved in the elementary reactions of complex decomposition processes [7]. The isotopic labelling was done by substituting the hydrogen (protium) atoms of the amino group with deuterium. Their results showed that deuterated TATB reacts 1.5 times slower than protonated TATB (i.e., $k_H/k_D \sim 1.5$) due to the kinetic-isotope-effect (KIE). The KIE occurs due to an increase in mass (e.g., from H to D), which reduces the vibrational energy of the bond (i.e., lower zero-point-energy) and thus increases the bond dissociation energy, requiring more time for the reactions to occur [25,26]. Even though Rogers et al. reported the KIE, they could not determine which specific pathways of TATB

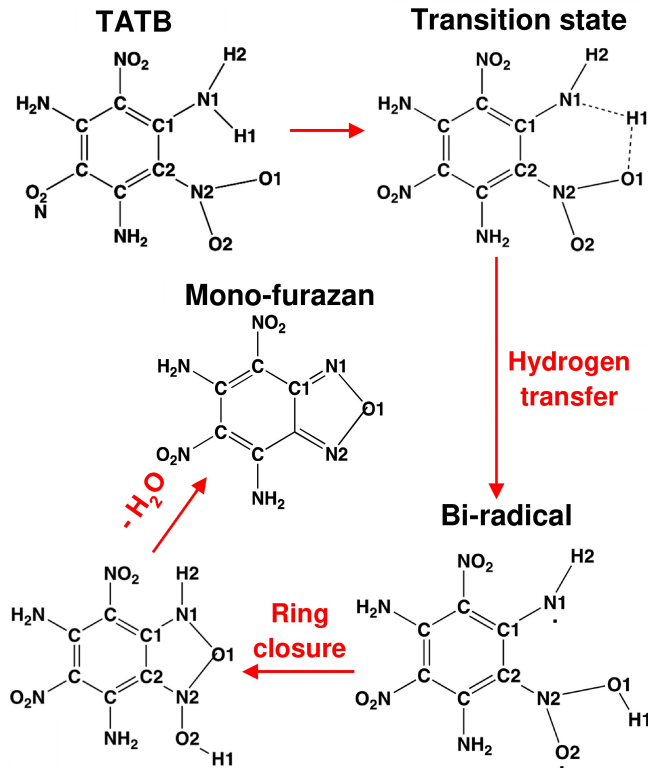


Figure 2. The most energetically favored endothermic pathway of TATB decomposition as determined by DFT calculations [24]. The intra-molecular hydrogen transfer mediated by ring closure forms a mono-furazan derivative of TATB and a water molecule. This pathway was reported as the rate-limiting step of TATB decomposition.

decomposition were affected by the KIE, because they did not perform chemical speciation measurements.

In this study, real-time chemical speciation measurements are performed with unsubstituted TATB and isotopically substituted TATB samples in separate experiments to differentiate the experimental signals during decomposition and to better elucidate the decomposition pathways and chemical species associated with those steps. We use infrared absorption spectroscopy to measure the evolution of chemical species as a function of time, to determine which decomposition products/pathways are affected by isotopic substitution, and to quantify the KIE. The thermal decomposition kinetics of TATB and deuterated TATB samples are also compared to those of the plastically bonded TATB-based explosive (LX-17) to understand the effect of the polymeric binder on the kinetics of chemical evolution.

2 Experimental Section

2.1 Chemical Speciation, Temperature, and Pressure Measurements

Figure 3a shows the schematic of the experimental setup used in the present study. The infrared spectra of chemical species were recorded using a Fourier Transform Infrared (FTIR) Spectrometer (*Bruker, Tensor II*). A globar light source from the FTIR passes through a 3-cm path length cell (*Specac, HTHP cell*) with ZnSe windows installed on both sides for line-of-sight measurements. The light intensity is measured using a liquid nitrogen cooled Mercury-Cadmium-Telluride (MCT) detector. A neutral density filter (*Thorlabs, NDIR10 A*) was placed between the cell and detector to minimize thermal emission from the hot gases that were produced during decomposition. Before each experiment, the sample cell was evacuated using a dry scroll pump and then purged with nitrogen gas three times to minimize interference from atmospheric species (e.g., CO₂, H₂O, etc.). Then, a reference spectrum, $I_{ref}(\nu)$, was recorded using the FTIR. The IR spectra of the gas-phase decomposition products, $I_{sample}(\nu)$, were acquired as a function of temperature and pressure during heating of the sample.

The intensity ratio, $I_{sample}(\nu)/I_{ref}(\nu)$, was calculated to determine the absorption spectrum from the Beer-Lambert law, $\alpha_\nu = -\ln(I_{sample}(\nu)/I_{ref}(\nu))$, where α_ν is the absorbance at wavenumber ν . The spectral data was acquired over the wavenumber range of 600–4000 cm⁻¹ with 1-cm⁻¹ resolution.

Pressed samples of TATB, LX-17, and deuterated TATB were used in this study. The pressed sample was weighed before the experiments using a 0.1- μ g resolution micro-balance (*Mettler Toledo, Comparator XPR6 U*). The sample was placed inside an aluminum crucible of 40- μ l volume (a sample capsule intended for DSC measurements). A press was used to seal an aluminum lid on to the crucible. The lid was then pierced to make a pin hole of approximately ~1-mm diameter. A

type-K thermocouple with an accuracy of ± 1.1 °C (*Omega Engineering-KMQSS*) was placed through the pin hole and positioned inside the aluminum crucible for direct measurements of the sample temperature as shown in Figure 3b. A data acquisition (DAQ) board (*National Instruments NI-9210* and *cDAQ-9171*) was used to record the temperature data. The temperature measurement error of the DAQ board was ± 0.7 °C, including gain, offset, differential, integral non-linearity, quantization, and noise errors. The overall uncertainty in temperature measurements was ± 1.8 °C. An exposed junction thermocouple was used to achieve fast response time (time constant of 0.3 s). The heating rates and operating temperatures of the cell body and window area were monitored by separate thermocouples and controlled by temperature controllers (*West Instruments, 6100*). The pressure in the cell was recorded using a pressure transducer (*Kulite, XTEH-7L-190-3000A*), a signal conditioner (*Kulite, KSC-2*), and another DAQ board (*National Instruments NI-USB-6211*). The uncertainty in pressure measurement was $\pm 0.1\%$ of the full-scale output ($\pm 20,265$ Pa), including non-linearity, hysteresis, and non-repeatability errors. Thermal error was eliminated by cooling the transducer via the Specac cell. A Labview code enables simultaneous acquisition of temperature, pressure, and spectral data.

TATB sublimation was observed on the ZnSe windows when preliminary tests were performed without an aluminum crucible. The sublimation should be minimized during the experiments to obtain reliable decomposition data. Therefore, the experiments were performed using aluminum crucibles with a small pin hole (1-mm diameter) to suppress sublimation. Figure S1 in Supplementary Information shows the IR spectra of materials deposited on the ZnSe windows without the lid and with the pinhole lid. Clearly the spectral features from solid TATB [27, 28] were suppressed with the lid, indicating sublimation was minimized.

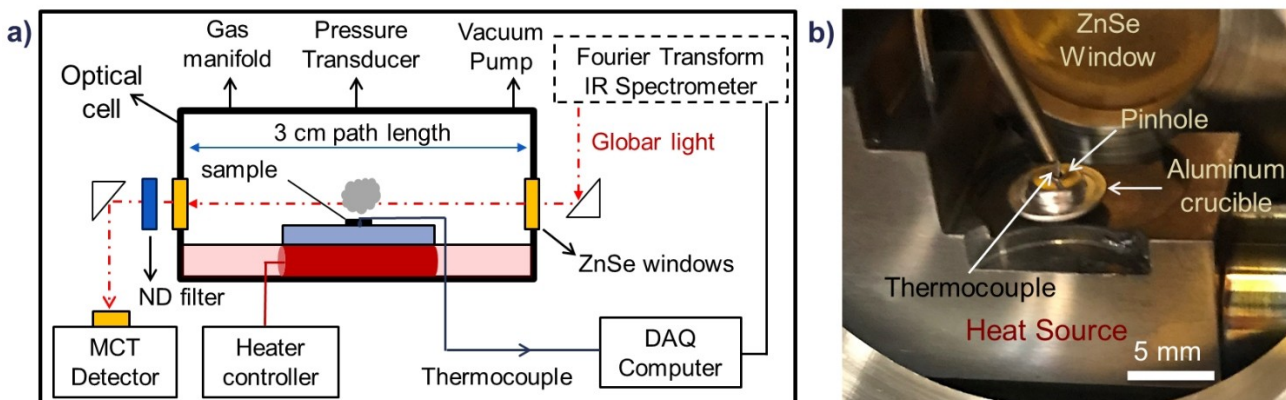


Figure 3. (a) The schematic of the experimental setup used for chemical speciation measurements during TATB decomposition. (b) Close-up view of the interior of the cell showing the aluminum crucible that contains the sample.

2.2 Experimental Conditions

The experimental conditions are summarized in Table 1. Three different samples were tested: TATB, deuterated TATB, and LX-17. The experiments were performed by heating nominally 2.5 mg of HE samples at a rate of 10 °C/min in a sealed cell filled with N₂ gas. The starting gas pressure ($\sim 5 \times 10^5$ Pa) was set to higher than atmospheric pressure to help minimize sublimation of the HE samples.

Figures 4a and b show the sample temperature and cell pressure recorded as a function of time during heating of the TATB sample (Test I in Table 1), respectively. The windows of the cell were heated first to prevent sublimation on the windows, and then the sample was heated at a rate of 10 °C/min until a temperature excursion was observed. The effects of excursion are displayed in the insets of Figures 4a and b. The sample temperature suddenly increased from 370 °C to 396 °C, whereas the effect on cell pressure was less pronounced. The isothermal decomposition experiments (Tests III to XII in Table 1) were performed below this excursion point to prevent self-heating of the samples to thermal runaway.

Figures 5a and b show the sample temperature and cell pressure recorded as a function of time during isothermal heating of the TATB sample (Test V in Table 1), respectively. The windows of the cell were heated first to prevent sub-

limation on the windows. After that, the sample was heated at a rate of 10 °C/min up to 331.8 °C and then the temperature was held constant for 2 hours. After isothermal conditions were achieved, the temperature fluctuations were ± 0.2 °C (i.e., no excursion) and the pressure was around 8.4×10^5 Pa ($\pm 1.2 \times 10^4$ Pa). The same heating procedure was followed for the other isothermal decomposition tests (Tests III to XII in Table 1) to minimize the self-heating of the samples.

2.3 Data Processing

Figure 6a shows an example spectrum acquired during isothermal decomposition of TATB at 331.8 °C. The absorption features due to CO₂, HCN, and NH₃ can be identified in the figure. The IR spectra of water molecules, H₂O, HDO, and D₂O (not shown) are discussed in detail in the results section. HNCO is another decomposition product observed during the experiments. Detection of low concentrations of HNCO is problematic because of overlap with CO₂ and H₂O features. Figure 6b shows the expanded range between 2200 and 2400 cm⁻¹. The spectra of three chemical species are displayed in the figure to discern the HNCO feature. H₂O (green line) and CO₂ (black line) are simulated using the HITRAN database [29], whereas the HNCO spectrum (blue

Table 1. Summary of Experimental Conditions.

Test No	Sample	Initial Mass [mg]	Initial Pressure [Pa]	Isotherm Temperature [°C]	Isotherm Duration [min]	Isotherm Pressure [Pa]
I	TATB	2.598				
II	Deuterated TATB	2.546	4.8×10^5	Ramp only	N/A	N/A
III	TATB	2.462		331.5	240	
IV	TATB	2.467		331.6		
V	TATB	2.578		331.8		
VI	TATB	2.485		332.1		
VII	Deuterated TATB	2.660		331.8		
VIII	Deuterated TATB	2.626	5.2×10^5	330.8	120	8.4×10^5 $\pm 1.2 \times 10^4$
IX	Deuterated TATB	2.658		332.0		
X	LX-17	2.429		331.1		
XI	LX-17	2.501		319.7		
XII	LX-17	2.425		340.3		

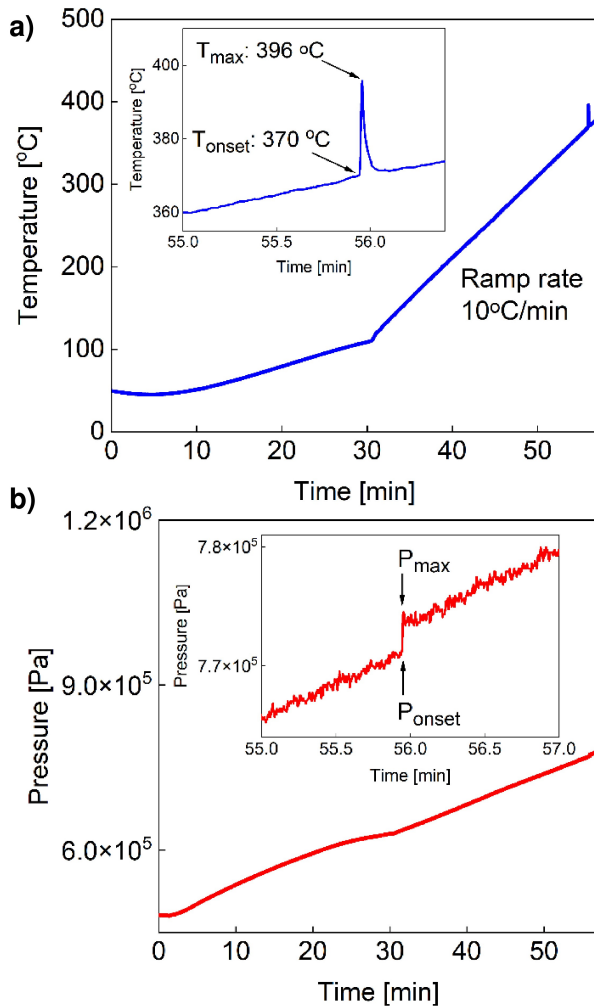


Figure 4. (a) The sample temperature and (b) cell pressure recorded as a function of time during a typical decomposition test of TATB. The sample was heated at a rate of $10^{\circ}\text{C}/\text{min}$ until a temperature excursion was observed. The insets show the effects of excursion on temperature and pressure histories.

line) is taken from a study in the literature [30]. The measured spectrum in this study compares quite well to the experimental measurement of pure HNCO gas produced from the reaction of sodium cyanate (NaOCN) with hydrogen chloride gas (HCl) [30].

The spectral data acquired as a function of time, temperature, and pressure were processed using a MATLAB script to determine the chemical evolution of the decomposition products. Each spectrum was integrated over specific wavenumber ranges: 2300 cm^{-1} to 2380 cm^{-1} for CO_2 , 963 cm^{-1} to 968 cm^{-1} for NH_3 , 712 cm^{-1} to 715 cm^{-1} for HCN , and 2230 cm^{-1} to 2260 cm^{-1} for HNCO. The integrated absorbance obtained from each spectrum was divided by the maximum integrated absorbance to report the normalized concentrations as a function of time. The noise in the measured absorbance (± 0.001) is used to estimate the un-

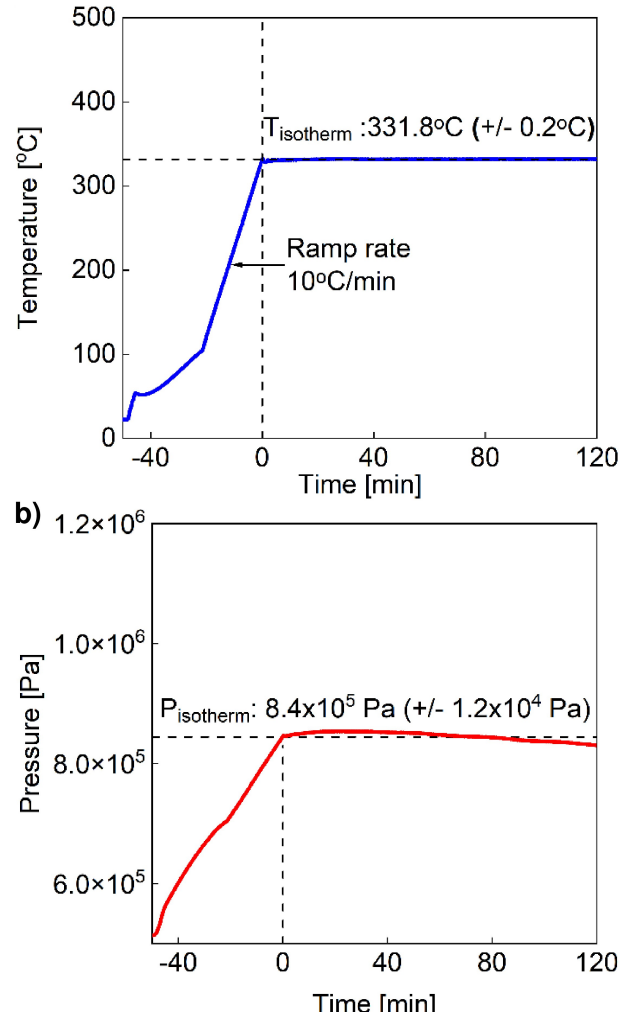


Figure 5. (a) The sample temperature and (b) cell pressure recorded as a function of time during a typical isothermal decomposition test of TATB. The sample was heated at a rate of $10^{\circ}\text{C}/\text{min}$ up to 331.8°C and then held at constant temperature for 2 hours.

certainties in normalized concentration measurements: $\pm 1\%$ for CO_2 , $\pm 2.5\%$ for HCN , $\pm 10\%$ for NH_3 , and $\pm 20\%$ for HNCO. The real-time chemical speciation data are shown in the results section.

2.4 Samples

The TATB used in this work has a purity of 98% as measured by high performance liquid chromatography. LX-17 is a plastically bonded explosive consisting of 92.5 weight % TATB and 7.5 weight % Kel-F 800. Kel-F 800 is a 3:1 copolymer of chlorotrifluoroethylene and vinylidene fluoride. The deuterated TATB samples were prepared by amination of 1,3,5-trichloro-2,4,6-trinitro-benzene (TCTNB) with deuterated ammonia (ND_3) according to the reaction scheme

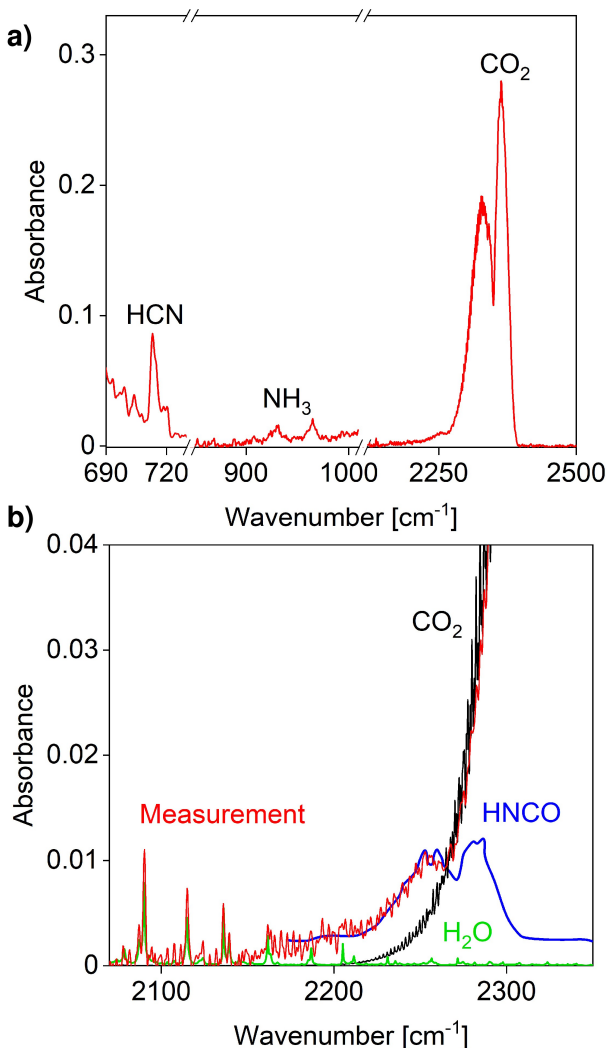


Figure 6. (a) An example infrared spectrum recorded during isothermal decomposition of TATB at 331.8 °C and at a time of $t = 37.5$ min with respect to the establishment of the isotherm. HCN, NH₃, and CO₂ are the decomposition products identified in the spectrum. (b) A close-up view of the spectrum shown in (a). The measured spectrum is shown by the red line. The spectra of three chemical species are displayed in the figure to discern the HNCO feature. H₂O (green line) and CO₂ (black line) are simulated using the HITRAN database [29], whereas the HNCO spectrum (blue line) is taken from a study in the literature [30].

shown in Figure S2 in Supplementary Information. The chemical purity of the deuterated TATB samples was 97%.

The isotopic purity of deuterated TATB samples was determined using ¹H magic angle spinning (MAS) Nuclear Magnetic Resonance (NMR) spectroscopy. Samples of deuterated and normal isotopic TATB were loaded into 1.3 mm (o.d.) rotors and then their masses were recorded (4.3 and 3.2 mg, respectively). The ¹H MAS NMR spectra were collected at a spinning rate of 50 kHz on a Bruker Avance 600 at an operating frequency of 600.099 MHz using a pulse delay of 2000 s for 16 scans each. Prior measurements of the

¹H T₁ via saturation recovery produced a value of 230 s for TATB, and the 2000 s pulse delay is more than 5 times the T₁ to ensure quantitative results. Figure S3 in Supplementary Information shows the recorded NMR spectra of TATB and deuterated TATB samples. The main peak for the NH₂ groups in TATB at 11.5 ppm was integrated for both spectra. Additional peaks from solvent and impurities outside the TATB can be observed from 0 to 6 ppm and were excluded in the analysis. The intensity for the normal isotopic TATB was used in combination with its mass to calibrate the ¹H NMR intensity to moles of ¹H in the sample. This value was then used to calculate the number of moles of normal isotopic TATB contained in the deuterated sample using its ¹H spectrum and mass. The final isotopic purity of the deuterated TATB (TATB-ND₂) was determined to be 95.6% using this method (the remainder was TATB-NH₂).

3 Results and Discussion

3.1 Chemical Speciation of TATB, LX-17, and Deuterated TATB

Figure 7a and b show the concentrations of decomposition products of TATB and LX-17 (Tests V and x in Table 1) as a function of time, respectively. The concentrations of CO₂, HNCO, and HCN molecules gradually increase and then rise steeply at a similar rate after the onset of the isotherm at 331 °C (i.e., time = 0 in the x-axes of the figures). This behavior indicates the presence of autocatalytic reactions. The concentration of NH₃ increases at a different rate during the early stage of decomposition. As the reactions proceed, the concentrations of HNCO and HCN molecules reach a maximum and decrease thereafter, whereas those of NH₃ and CO₂ continue to increase. The latter two species achieve a similar rate of production after halfway through the decomposition process (i.e., ~70 minutes). The duration of the isothermal heating at 331 °C was extended to 240 minutes in a separate experiment (Test III in Table 1) to determine whether the chemical speciation patterns observed in Figures 7a and b would change after 120 minutes. The results are displayed in Figure S4 in Supplementary Information. The same trends of chemical evolution (i.e., CO₂ and NH₃ increase; HNCO and HCN decrease), were seen over a longer period of time.

Before performing the decomposition tests the experimental setup used in this study is evacuated and purged with N₂ gas at room temperature in order not to influence the HE decomposition kinetics by vacuuming the setup at higher temperatures. However, after the temperature exceeds 100 °C during heating of the setup, the surface-absorbed atmospheric water of the setup volatilizes and mixes with the water produced later at higher temperatures due to sample decomposition. Figure 8a compares the IR spectrum recorded during heating of an empty cell without any HE samples to that acquired with TATB to de-

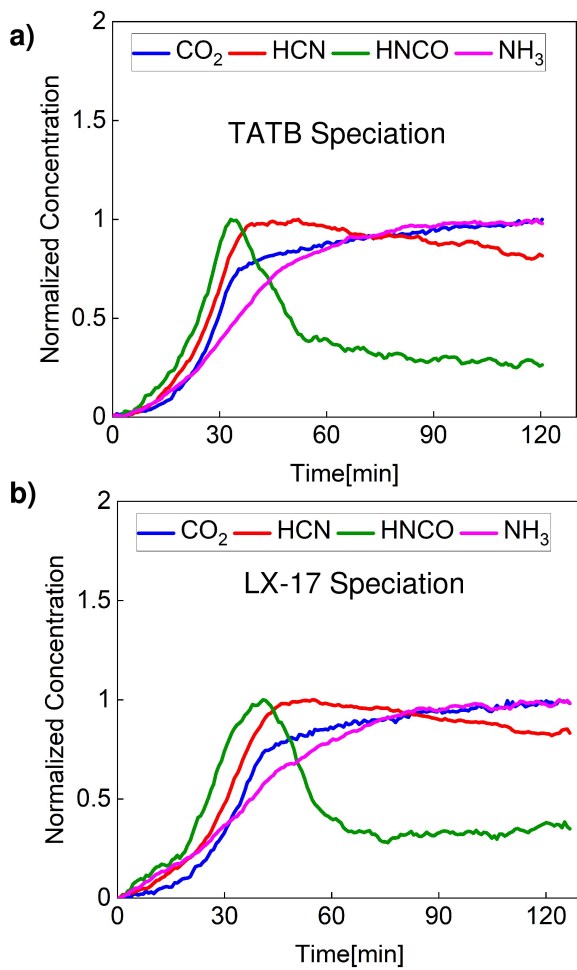


Figure 7. Concentrations of CO₂, HCN, HNCO, and NH₃ molecules as a function of time at 330 °C during isothermal decomposition of (a) TATB and (b) LX-17.

determine the atmospheric water contribution. The water absorption is clearly higher when a TATB sample is present.

Also, the H₂O spectrum is simulated at 330 °C using the HITRAN database [29] to verify all the measured absorption features are due to the water molecule. We observed slight variations in the amount of water vapor produced from an empty cell on different days of testing. For that reason, the chemical speciation of deuterium labeled TATB samples is investigated to definitively identify the water vapor evolution due to sample decomposition.

Figure 8b compares the measured IR spectra of gas-phase decomposition products of TATB and deuterated TATB to the simulated infrared spectra of water (H₂O), deuterated water (HDO), and heavy water (D₂O). The spectra of water molecules are taken from the HITRAN database [29]. As expected, the IR spectrum acquired during TATB decomposition does not have any features pertinent to deuterium. The IR spectrum recorded during deuterated TATB decomposition shows HDO. The OH and H radical abstractions

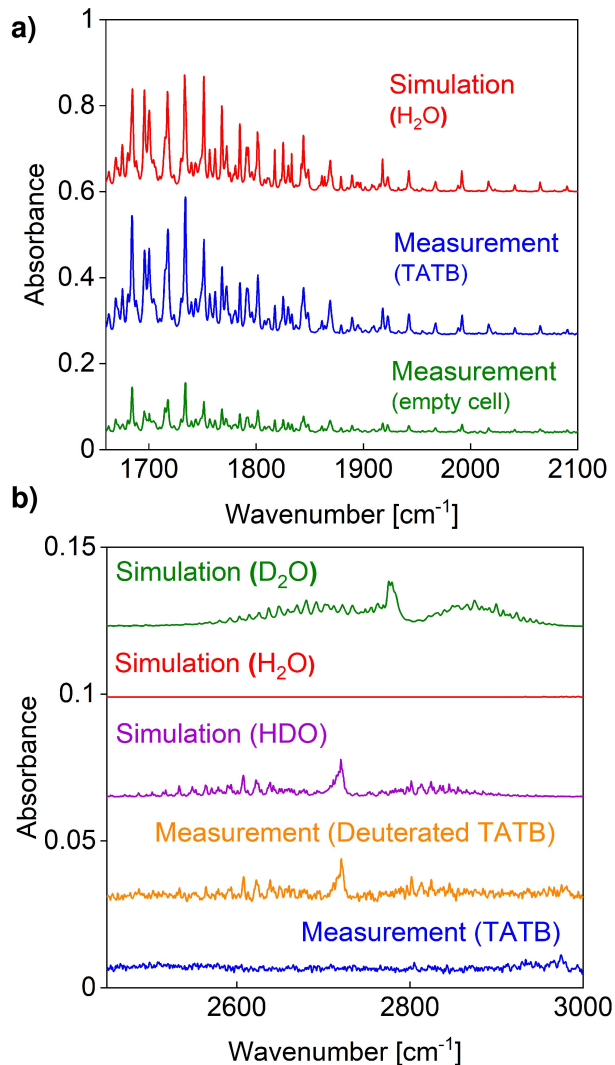


Figure 8. (a) The infrared spectrum of H₂O at 330 °C is simulated using the HITRAN database and compared to the measured spectrum recorded at the end of the 2-hour isothermal decomposition of TATB at 330 °C. The IR spectrum recorded after heating the empty cell without any HE sample is also included in the figure. (b) The simulated infrared spectra of D₂O, HDO, and H₂O are compared to those measured at the end of the 2-hour isothermal decomposition of TATB and deuterated TATB. The frequencies of the spectral features are compared to definitively identify the measured chemical species (e.g., HDO).

from TATB form a water molecule during decomposition as suggested in Figure 2. Similarly, D₂O formation would be expected in the presence of OD and D radicals during deuterated TATB decomposition. However, D₂O formation might be preceded by a hydrogen-deuterium exchange and result in HDO formation, because the energy barriers for these type of isotope exchanges are very low (e.g. E_a = 4.13 kcal/mol (17.3 kJ/mol) at 100 °C for H₂O + OD → HDO + OH) [31] compared to the overall activation energy of TATB. D₂O formation might also be proceeded by an isotope ex-

change, resulting in HDO formation (e.g. $\text{OH} + \text{D}_2\text{O} \rightarrow \text{HDO} + \text{OD}$) [31]. In summary, the presence of HDO is associated with an isotope exchange reaction, which could happen through different routes.

Figure 9 shows the concentrations of decomposition products of deuterated TATB (Test VII in Table 1) as a function of time. The HDO formation precedes the formation of the other molecules. This is consistent with the first steps of TATB decomposition forming water [18, 24]. HNCO and HCN molecules form after HDO, and then the concentrations of NH_3 and CO_2 increase around the same time. As the concentrations of HDO, HCN, and HNCO decrease, those of NH_3 and CO_2 increase. Figure 9 also shows HDO was not detected until the deuterated TATB temperature reached nearly 330°C . This means the hydrogen/deuterium exchange occurred after the sample started thermally decomposing. The spectral signatures of the deuterated analogues of NH_3 , HCN, and HNCO molecules (e.g., ND_3 , ND_2H , DCN, DNCO) [32–41] were not observed during real-time chemical speciation measurements. Like the absence of the D_2O molecule, the absence of molecules such as ND_3 could be due to the rapid hydrogen-deuterium exchange reactions, resulting in small concentrations of deuterated species (e.g., DCN, NH_2D , ND_2H) and thus preventing their detection.

The path length of the gas cell used for the real-time chemical speciation measurements was 3 cm. A separate gas cell with a 1-m path length (*Bruker, A137*) was used to measure trace gases at the end of deuterated TATB and TATB decomposition experiments to determine if the decomposition products included deuterated species such as D_2O and DCN. The cell was located inside the FTIR spectrometer and kept at room temperature. The gas-phase decomposition products of TATB and deuterated TATB (Tests I

and II in Table 1) were transferred from the 3-cm path length cell to the 1-meter path length cell in separate experiments, and then the IR spectra were recorded. The spectral features of D_2O , HDO (see Figure S5), and DCN (see Figure S6 in Supplementary Information) were identified in the measured spectrum of deuterated TATB decomposition products. Figure S5b shows the measured HDO absorbance is an order of magnitude higher than that of D_2O . The absorption coefficients of HDO and D_2O are similar in this wavelength range [29]. Therefore, the concentration of D_2O is expected to be an order of magnitude smaller than that of HDO, which should be the reason why D_2O detection was problematic with a 3-cm path length cell.

The use of the 1-m path length cell allowed us to identify three other species in the measured spectra of TATB and deuterated TATB decomposition products. These species include: NO (see Figure S7), N_2O , and CO (see Figure S8). The CO_2 spectral features overlap with those of HNCO at room temperature (Figure S8), preventing its definitive identification. Similarly, the N_2O features are spectrally located where DNCO is IR active [42, 43] (Figure S8). The NH_3 (or ND_3 , ND_2H , NH_2D) detection at room temperature is also problematic in the presence of H_2O and CO_2 , because ammonia precipitates in the form of NH_4HCO_3 [44]. Even though the path length of the cell was 1 m, Figure S9 in Supplementary Information shows the measured NH_3 absorbance at room temperature was only 0.01. This absorbance value is almost the same as the one measured by our 3-cm path length cell (see Figure 6a). This result highlights the importance of our real-time chemical speciation measurements for identifying molecules such as NH_3 at high temperatures.

In summary, we measured the following decomposition products in real time using the 3-cm path length cell: HDO, CO_2 , HCN, HNCO, and NH_3 . We also measured five other species using the 1-m path length cell at the end of the decomposition tests: NO, N_2O , CO, DCN, and D_2O . It is important to understand which chemical species are the major decomposition products. The absorption cross sections are available for all the measured chemical species except for HNCO [29]. Table 2 summarizes the concentrations of the gas-phase products calculated using our measured absorbance data at the end of TATB and deuterated TATB decomposition experiments (Tests I and II in Table 1).

The results obtained from the 3-cm path length cell in Table 2 show that CO_2 concentration is almost the same for both TATB and deuterated TATB, whereas HCN and NH_3 concentrations are slightly less for deuterated TATB, as expected. HDO concentration (803 ppm) is higher than those of the other species. Although not shown in the table, the H_2O concentration was calculated to be 1936 ppm at the end of TATB decomposition. As discussed earlier in this section, the surface adsorbed atmospheric water also contributes to H_2O formation and it is clear from these results that the amount of environmental water is comparable to that coming from the sample, and thus it could provide the hy-

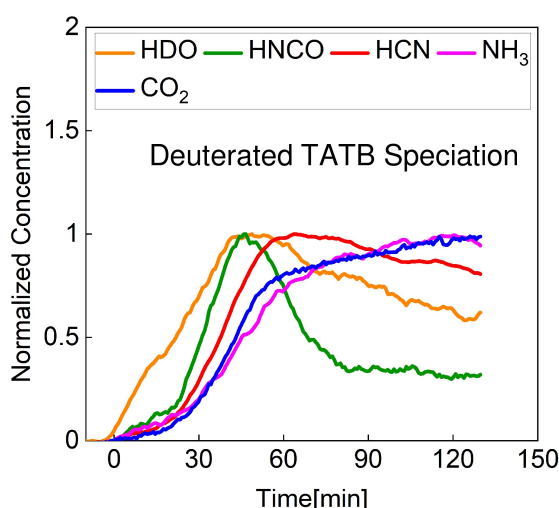


Figure 9. Concentrations of CO_2 , HCN, NH_3 , HNCO, and HDO as a function of time during thermal decomposition of deuterated TATB at 330°C . HDO forms first, followed by HNCO, HCN, NH_3 , and CO_2 .

Table 2. Concentrations of product-gases at the end of TATB and deuterated TATB decomposition experiments (Tests I and II in Table 1).

Product Gas	Concentration in the 3-cm cell [ppm]		Concentration in the 1-m cell [ppm]	
	TATB	Deuterated TATB	TATB	Deuterated TATB
CO ₂	505	498	191	199
HCN	998	778	342	315
NH ₃	143	112	—	—
HDO	—	803	—	641
D ₂ O	—	—	—	45
NO	—	—	347	341
N ₂ O	—	—	7	6
CO	—	—	108	107

drogen for H/D exchange. In a future study, the 3-cm path length cell could be vacuumed slightly above 100 °C to completely remove the surface adsorbed water contribution. In the present study, we did not follow this procedure in order not to influence the rate of the decomposition process, because TATB could sublime under vacuum pressures at temperatures higher than room temperature. TATB could also be sensitized at high temperatures, influencing the decomposition kinetics.

The results obtained from the 1-m path length cell in Table 2 show that the concentrations of chemical species are smaller than those obtained from the 3-cm path length. This is due to the increase in volume as the gases are transferred to the 1-m path length cell. The results also show that NO and HCN concentrations are almost the same, whereas CO concentration is half of that of CO₂ and N₂O concentration is only 6–7 ppm. This means CO and NO are two other major decomposition products, whereas N₂O is a minor species. In addition, NH₃ was not identified due to the precipitation of NH₃ in the form of NH₄HCO₃ at room temperature.

At the end of the HE decomposition tests, solid residues remained in the aluminum crucibles. The weights of the samples were measured before and after the decomposition tests to determine the weights of gas-phase products. The gas-phase products accounted for 84% of the starting material, which was nominally 2.5 mg as given in Table 1. The concentrations obtained from the 3-cm path length cell in Table 2 were used to calculate the weights of the gasses. The weight percent of the gasses were determined to be 1.5%, 13%, and 15% for NH₃, CO₂, and HCN, respectively. In a future study, the globar light source from the FTIR spectrometer could be arranged to make multiple passes through the 3-cm path length cell to be able to measure the weight percent of the other major decomposition products in real time (e.g., NO and CO). In this way, we might also measure other chemical species (e.g., C₂N₂, C₄N₄O) identified in mass spectrometry measurements [8, 10, 18, 44–47]. Those heavier molecules were not observed in IR spectroscopy studies [3, 9].

3.2 The Comparison of Thermal Decomposition Kinetics for TATB, LX-17, and Deuterated TATB

Figures 10 (a) and (b) compare the evolution of CO₂ and HCN molecules, respectively, during isothermal decomposition of TATB, LX-17, and deuterated TATB at nominally 330 °C. The trends in evolution are very similar for all the samples, but their kinetic behaviors are different. This indicates the rates of consistent pathways are changed during thermal decomposition. The chemical evolution of LX-17 is slightly slower than that of TATB. This could be due to the polymeric binder in LX-17. The formation of CO₂ and HCN is even slower for the deuterated TATB sample. Figures 10 (c) and (d) compare the evolution of NH₃ and HNCO molecules, respectively, during thermal decomposition of TATB, LX-17, and deuterated TATB at nominally 330 °C. The changes in the kinetics of NH₃ and HNCO formation due to the KIE were similar to those observed for CO₂ and HCN, whereas the differences between TATB and LX-17 were less pronounced.

The kinetics of chemical evolution for three different samples are more quantitatively compared by determining the time at which the maximum rate of CO₂ production is achieved during decomposition. The reciprocals of the ratios of the time values are reported as the ratios of the rates. The comparison shows that the kinetics of deuterated TATB decomposition is slower than that of TATB (e.g., k_H/k_D ~ 1.41). The rate of LX-17 decomposition lies in between those of TATB and deuterated TATB ($k_{\text{TATB}}/k_{\text{LX-17}} \sim 1.15$).

The results displayed in Figure 10 also show the KIE is more pronounced during the early stages of deuterated TATB decomposition (i.e., before the maximum rate of chemical evolution occurs). The early influence of the KIE could be due to the first steps of TATB decomposition forming water and mono-furazan via intra-molecular hydrogen transfer (as opposed to deuterium transfer) [24]. Figure 10 also shows the kinetics of LX-17 decomposition is slightly slower than that of TATB. The slower gas release from LX-17 decomposition could be due to the polymeric binder, Kel-F. Kel-F is known to exhibit endothermic thermal decomposition behavior with an activation energy of 271 kJ/mol [48], which is slightly higher than those reported for TATB thermal decomposition (210 kJ/mol) [5–11]. Although Kel-F melts before TATB decomposes, it decomposes nearly 100 °C higher than TATB [48]. Kel-F is also

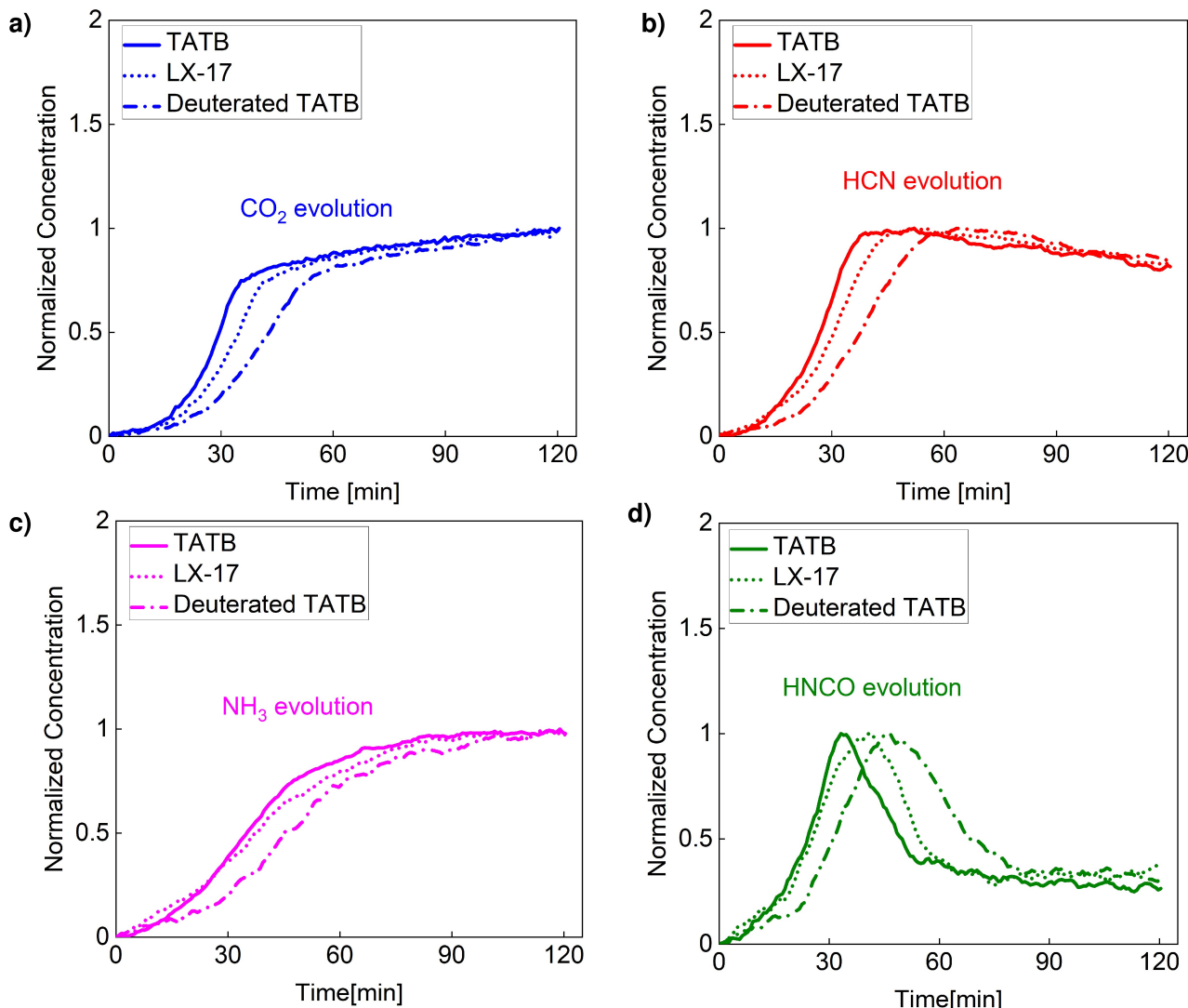


Figure 10. Comparison of evolution of (a) CO₂, (b) HCN, (c) NH₃, and (d) HNCO molecules during isothermal decomposition of TATB, LX-17, and deuterated TATB at 330°C and 8.4 × 10⁵ Pa.

known to enhance the likelihood of self-heating of LX-17 for high heat-flow conditions, perhaps by slowing the release of autocatalytic species by acting as a diffusion barrier during thermal decomposition [49]. For the low heat-flow conditions of the experiments here, self-heating is not a problem, but any such diffusion resistance would still be important for release of the gas species.

The KIE observed in the current study is very close to that obtained from the DSC measurement results ($k_H/k_D \sim 1.5$) [7]. The thermal decomposition tests at 330 °C were repeated under the same conditions with TATB (Tests IV and VI in Table 1) and deuterated TATB samples (Test VIII and IX in Table 1) to verify the repeatability of the results. The CO₂ evolution measured during six different tests are displayed in Figure S10 in Supplementary Information. The (k_H/k_D) values derived from different tests varied only by ± 5 %.

3.3 The Effect of Temperature on Chemical Evolution of Decomposition Products

The concentration time histories of chemical species are also recorded during isothermal decomposition of LX-17 at two other temperatures: 320 °C and 340 °C (Tests XI and XII in Table 1).

Figures 11a through d compare the evolutions of CO₂, HCN, NH₃, and HNCO, respectively, at three different temperatures. The effect of temperature on the kinetics of evolution was very similar for all molecules. As the isothermal decomposition temperature was changed from 320 °C to 330 °C, a substantial increase in the rate of evolution was seen, whereas the increase in the rate of evolution was less pronounced when the sample temperature was changed from 330 °C to 340 °C. This indicates the formation mechanism of all four spe-

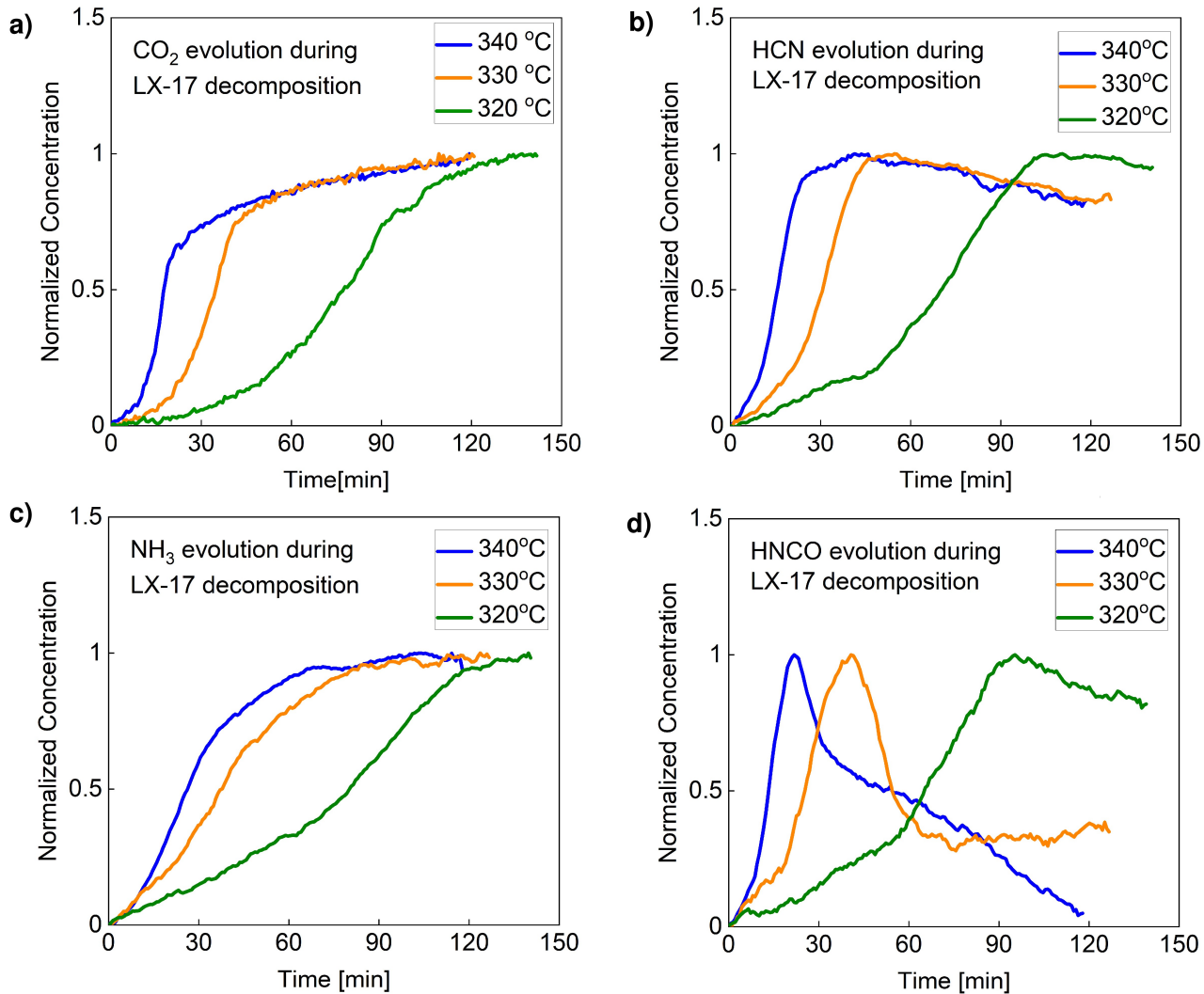


Figure 11. Comparison of (a) CO₂, (b) HCN, (c) NH₃, and (d) HNCO evolutions during isothermal decomposition of LX-17 at three different temperatures (320 °C, 330 °C, and 340 °C).

cies might be a part of a series of decomposition pathways (that might be similarly affected by temperature changes) rather than a set of independent and parallel pathways.

The speciation results displayed in Figure 11 indicate that the concentrations rise rapidly (i.e., burst period) after a short induction period, which is typical for autocatalytic reactions. The CO₂ concentration time histories in Figure 11a exhibit sigmoidal-shaped kinetics ("S-shaped curves") that are similar to those reported in the literature for solid-phase autocatalytic reactions [50]. Therefore, the measured CO₂ concentration time histories are fit to the autocatalytic rate expressions derived in a previous study [51]. The expressions are explained in detail in Supplementary Information (Equations 1 to 5). Figure S11 in SI compares the measurement results to the fits at different temperatures. Figure S11 shows the auto-catalytic behavior of CO₂ evolution is well represented by the sigmoid fit. However, a significant deviation from the sigmoid fit occurs

after the induction and burst periods. The deviation becomes more pronounced as the temperature increases from 320 °C to 340 °C. This indicates that a third mechanism of CO₂ formation begins after the end of the autocatalytic reactions. The thermal decomposition reactions of TATB are known to leave behind carbon-and nitrogen-containing solid products [52,53]. The carbonaceous residues might react with the surrounding water and generate CO₂ gas. This gasification reaction could be the third mechanism of CO₂ formation. Nevertheless, the reactant chemical species that acts as the catalyst is currently unknown. Therefore, it would be desirable in future to examine the catalytic effects of different chemical species on decomposition kinetics. This would also allow a more comprehensive and quantitative understanding of the rate parameters obtained from the fits.

The rate parameters shown in the Supplementary Information could be used to determine the activation energies

of the autocatalytic reactions for LX-17. However, in the present study the rate parameters are available only at three different temperatures. Therefore, we recommend taking more data as a function of temperature and ramp rate to accurately report the activation energies in a future study. In addition, this could be done for both TATB and LX-17 to more quantitatively compare the kinetic parameters.

3.4 Discussion on Decomposition Mechanisms

The carbon contained in the HNCO, HCN, and CO₂ molecules must come from the central aromatic ring of TATB. A mechanism for this full decomposition pathway does not exist in the literature. Figure 9 shows that water concentration begins to rise more rapidly than the other monitored gases, consistent with an initial water elimination reaction. The KIE also supports that hydrogen transfer must occur before formation of light gases, which are all delayed significantly in deuterated samples. After this reaction to form a furazan or furoxan species, we propose that this newly formed secondary ring may open at one of the N–O bonds and cause a zipper-like rearrangement of bonds around the central ring. Ultimately, this could rupture the central ring and free the two carbon atoms previously part of both the central and side rings. Each carbon atom would however still be connected to their neighboring nitrogen atom and any oxygen bonded to it. These cyanide or fulminate anions could then easily strip a hydrogen atom from a nearby amine group to form hydrogen cyanide and fulminic acid. The fulminic acid would then rapidly tautomerize to the more energetically favorable isocyanic acid [54]. These species can then further react with water to decompose into ammonia and carbon dioxide or monoxide [30]. The concentration patterns shown in Figures 7 and 9 support this mechanism where H₂O, HCN and HNCO peak early but then begin to decompose further into the final products (e.g., CO₂, NH₃). However, there could be other decomposition mechanisms involving different reactions. Therefore, theoretical calculations (e.g., DFT) could be done in a future study to determine the most energetically favored decomposition pathways. Also, the heavier molecules such as furazans were not detected in the present study. They were not detected in other IR spectroscopy measurements either [3,9]. As suggested earlier in this paper, the globar light source from the FTIR spectrometer could be arranged to make multiple passes in a future study to improve the detection limits and to be able to measure the heavier molecules in real time during TATB decomposition.

4 Conclusions

In-situ chemical speciation measurements were performed during thermal decomposition of unsubstituted TATB and deuterated TATB samples to differentiate the experimental signals with the help of isotopic substitution and to better de-

lineate the decomposition pathways. The experiments were also conducted with plastically bonded TATB samples (LX-17) to measure the effect of the polymeric binder (Kel-F 800) on decomposition kinetics. The high explosive samples were thermally decomposed over 2 hours at isothermal conditions (e.g., 330 °C) in a sealed cell kept at 8.4 × 10⁵ Pa of N₂ gas. IR absorption spectroscopy was used to identify the gaseous decomposition products.

The time-resolved chemical speciation measurement results show that water first forms during decomposition, followed by the other molecules, including HNCO, HCN, NH₃, and CO₂. The concentration histories exhibit an autocatalytic behavior (i.e., a rapid rise after an induction period) during the early stages of decomposition. After the autocatalytic behavior is over, the concentrations of some gases change by a small amount and some remain constant: the concentration of CO₂ gradually increases, those of H₂O, HCN, and HNCO slightly decrease, whereas that of NH₃ becomes stable. This concentration pattern is attributed to the gasification reactions (e.g., formation of CO₂) in the presence of water from the carbonaceous residues of the decomposition products.

The rate of evolution of species are used to compare decomposition kinetics among different explosives. Deuterated TATB reacts 1.41 times slower than protonated TATB ($k_H/k_D \sim 1.41$) due to the kinetic-isotope-effect (KIE), whereas LX-17 reacts 1.15 times slower than pure TATB ($k_{TATB}/k_{LX-17} \sim 1.15$) due to the polymeric binder. The results varied by ±5% based on the repeatability of the experiments. The trends of chemical evolution are similar for all the samples, but their kinetic behaviors are different. This indicates the rates of consistent pathways are changed during thermal decomposition. The KIE is more pronounced during the early stages of deuterated TATB decomposition. This is attributed to the first steps of TATB decomposition involving water formation via intra-molecular hydrogen transfer (i.e., H vs D transfer).

The effect of temperature on thermal decomposition of LX-17 is also investigated by performing the tests at three different isotherms (320, 330, and 340 °C). The effect of temperature on evolution kinetics of individual species is similar for all molecules. This suggests the decomposition mechanism might involve a series of pathways that are similarly affected by temperature changes rather than a set of independent and parallel reactions. This conclusion is also supported by the KIE observed in this study. The KIE due to deuterium substitution slows down the formation of all gases during deuterated TATB decomposition, including those lacking hydrogen (e.g., CO₂).

Acknowledgements

This work was performed under the auspices of the U.S. Department of Energy by Lawrence Livermore National Laboratory under Contract DE-AC52-07NA27344. We are thankful to Franco Gagliardi for pressing the HE samples. We appreciate the works of our summer interns, Jor-

dan Combitsis and Marvin Sabas, who developed our MATLAB script to process large data sets. We thank Keith Coffee for the chemical purity measurements. We are also thankful to Libby Glascoe for her insightful discussions on TATB decomposition kinetics.

Data Availability Statement

No data available.

References

- [1] B. M. Dobratz, The insensitive high explosive triaminotrinitrobenzene (TATB): Development and characterization, 1888 to 1994, United States, Aug. **1995**. doi: 10.2172/90370.
- [2] S. F. Rice and R. L. Simpson, The unusual stability of TATB: A review of the scientific literature, Lawrence Livermore National Laboratory report UCRL-LR-103683, July 4, **1990**.
- [3] T. B. Brill, K. J. James, Thermal decomposition of energetic materials. 61. Perfidy in the amino-2,4,6-trinitrobenzene series of explosives, *J. Phys. Chem.* **1993**, *97*, 8752–8758. DOI 10.1021/j100136a017.
- [4] T. B. Brill, K. J. James, Kinetics and mechanisms of thermal decomposition of nitroaromatic explosives, *Chem. Rev.* **1993**, *93*, 2667–2692. DOI: 10.1021/cr00024a005.
- [5] R. N. Rogers, L. C. Smith, Application of scanning calorimetry to the study of chemical kinetics, *Thermochim. Acta* **1970**, *1*, 1–9. DOI: 10.1016/0040-6031(70)85023-7.
- [6] R. N. Rogers, Thermochemistry of explosives, *Thermochim. Acta* **1975**, *11*, 131–139. DOI: 10.1016/0040-6031(75)80016-5.
- [7] R. N. Rogers, J. L. Janney, M. H. Ebinger, Kinetic-isotope effects in thermal explosions, *Thermochim. Acta* **1982**, *59*, 287–298. DOI: 10.1016/0040-6031(82)87151-7.
- [8] E. Catalano, P. C. Crawford, An enthalpic study of the thermal decomposition of unconfined triaminotrinitrobenzene, *Thermochim. Acta* **1983**, *61*, 23–36. DOI: 10.1016/0040-6031(83)-80301-3.
- [9] P. S. Makashir, E. M. Kurian, Spectroscopic and thermal studies on the decomposition of 1,3,5-triamino-2,4,6-trinitrobenzene (TATB), *J. Therm. Anal.* **1996**, *46*, 225–236. DOI: 10.1007/BF01979963.
- [10] R. Belmas, A. Bry, C. David, L. Gautier, A. Keromnès, D. Poullain, G. Thevenot, C. Le Gallic, J. Chenault, G. Guillaumet, Preheating Sensitization of a TATB Composition Part one: Chemical Evolution, *Propellants, Explos., Pyrotech.* **2004**, *29*(5), 282–286. DOI: 10.1002/prep.200400059.
- [11] A. Singh, T. C. Sharma, M. Kumar, J. K. Narang, P. Kishore, A. Srivastava, Thermal decomposition and kinetics of plastic bonded explosives based on mixture of HMX and TATB with polymer matrices, *Def. Technol.* **2017**, *13*(1), 22–32. DOI: 10.1016/j.dt.2016.11.005.
- [12] R. R. McGuire, C. M. Tarver, Chemical Decomposition Models for the Thermal Explosion of HMX, TATB, RDX, and TNT Explosives, 7th Symposium (International) on Detonation, Naval Surface Weapons Center NSWC MP 82–334, Annapolis, MD, **1981**, pp. 56–63.
- [13] J. Sharma, J. W. Forbes, C. S. Coffey, T. P. Liddiard, Physical and chemical nature of sensitization centers left from hot spots caused in triaminotrinitrobenzene by shock or impact, *J Phys Chem U.S.* **1987**. DOI: 10.1021/j100303a053.
- [14] J. Sharma, W. L. Garrett, F. J. Owens, V. L. Vogel, X-ray photoelectron study of electronic structure, ultraviolet, and isothermal decomposition of 1,3,5-triamino-2,4,6-trinitrobenzene, *J. Phys. Chem.* **1982**, *86*(9), 1657–1661. DOI: 10.1021/j100206a034.
- [15] J. Sharma, J. C. Hoffsommer, D. J. Clover, C. S. Coffey, F. Santago, A. Stolovy, S. Yasuda, Comparative Study of Molecular Fragmentation in Sub-initiated TATB Caused by Impact, UV, Heat and Electron Beam, in: *Shock Waves in Condensed Matter* (Eds.: J. R. Asay, R. A. Graham, G. K. Straub), Elsevier, Amsterdam **1983**, pp 543–546. DOI: 10.1016/B978-0-444-86904-3.50123-8.
- [16] J. Sharma, B. C. Beard, M. Chaykovsky, Correlation of impact sensitivity with electronic levels and structure of molecules, *J. Phys. Chem.* **1991**, *95*(3), 1209–1213. DOI: 10.1021/j100156a032.
- [17] J. Sharma, F. J. Owens, XPS study of UV and shock decomposed triamino-trinitrobenzene, *Chem. Phys. Lett.* **1979**, *61*(2), 280–282. DOI: 10.1016/0009-2614(79)80644-2.
- [18] T. A. Land, W. J. Siekhaus, M. Foltz, R. Behrens Jr., Condensed-phase thermal decomposition of TATB investigated by atomic force microscopy (AFM) and simultaneous thermogravimetric modulated beam mass spectrometry (STMBMS), May **1993**, <https://www.osti.gov/servlets/purl/10191262>.
- [19] E. A. Glascoe, L. N. Dinh, W. Small, G. E. Overturf, Moisture Desorption Rates from TATB Formulations: Experiments and Kinetic Models, *J. Phys. Chem. A* **2012**, *116*(22), 5312–5316. DOI: 10.1021/jp303074g.
- [20] W. Small, E. A. Glascoe, G. E. Overturf, Measurement of moisture outgassing of the plastic-bonded TATB explosive LX-17, *Thermochim. Acta* **2012**, *545*, 90–95. DOI: 10.1016/j.tca.2012.06.033.
- [21] E. A. Glascoe, J. M. Zaug, M. R. Armstrong, J. C. Crowhurst, C. D. Grant, and L. E. Fried, Nanosecond Time-Resolved and Steady-State Infrared Studies of Photoinduced Decomposition of TATB at Ambient and Elevated Pressure, *J. Phys. Chem. A* **2009**, *113*(20), 5881–5887. DOI: 10.1021/jp809418a.
- [22] M. Farber and R. D. Srivastava, Thermal decomposition of 1,3,5-triamino-2,4,6-trinitrobenzene, *Combust. Flame* **1981**, *42*, 165–171. DOI: 10.1016/0010-2180(81)90155-3.
- [23] H. Ostmark, Shock induced sub-detonation chemical reactions in 1,3,5-triamino-2,4,6-trinitrobenzene, *9th Conference of the American Physical Society Topical Group on Shock Compression of Condensed Matter*, Seattle, Washington (USA), August 13–18, **1995**, AIP Conference Proceedings 370, p.871.
- [24] C. J. Wu and L. E. Fried, Ring Closure Mediated by Intramolecular Hydrogen Transfer in the Decomposition of a Push-Pull Nitroaromatic: TATB, *J. Phys. Chem. A* **2000**, *104*(27), 6447–6452. DOI 10.1021/jp001019r.
- [25] S. A. Shackelford, Condensed Phase Kinetic Deuterium Isotope Effects in High Energy Phenomena: Mechanistic Investigations and Relationships, Technical Report No: FJSRL-TR-89-0010, Frank J. Seiler Research Lab, United States Air Force, Dec. **1989**.
- [26] A. Sattler, Hydrogen/Deuterium (H/D) Exchange Catalysis in Alkanes, *ACS Catal.* **2018**, *8*(3), 2296–2312. DOI 10.1021/acscatal.7b04201.
- [27] T. G. Towns, Vibrational spectrum of 1,3,5-triamino-2,4,6-trinitrobenzene, *Spectrochim. Acta Part Mol. Spectrosc.* **1983**, *39*(9), 801–804. DOI 10.1016/0584-8539(83)80020-8.
- [28] B. L. Deopura and V. D. Gupta, Vibration Spectra of 1,3,5-Triamino-2,4,6-trinitrobenzene, *J. Chem. Phys.* **1971**, *54*(9), 4013–4019. DOI 10.1063/1.1675458.

- [29] L. S. Rothman, E. Gordon, Y. Babikov, A. Barbe, D. Chris Benner, P. F. Bernath, M. Birk, L. Bizzocchi, V. Boudon, L. R. Brown, A. Campargue, K. Chance, E. A. Cohen, L. H. Coudert, V. M. Devi, B. J. Drouin, A. Fayt, J.-M. Flaud, R. R. Gamache, J. J. Harrison, J.-M. Hartmann, C. Hillo, J. T. Hodges, D. Jacquemart, A. Jolly, J. Lamouroux, R. J. Le Roy, G. Li, D. A. Long, O. M. Lyulin, C. J. Mackie, S. T. Massie, S. Mikhailenko, H. S. P. Müller, O. V. Nauenko, A. V. Nikitin, J. Orphal, V. Perevalov, A. Perrin, E. R. Polovtseva, C. Richard, M. A. H. Smith, E. Starikova, K. Sung, S. Tashkun, J. Tennyson, G. C. Toon, Vl. G. Tyuterev, G. Wagner, The HITRAN2012 molecular spectroscopic database, *J. Quant. Spectrosc. Radiat. Transfer* **2013**, *130*, 4–50. DOI: 10.1016/j.jqsrt.2013.07.002.
- [30] M. S. Lowenthal, R. K. Khanna, M. H. Moore, Infrared spectrum of solid isocyanic acid (HNCO): vibrational assignments and integrated band intensities, *Spectrochim. Acta. A. Mol. Biomol. Spectrosc.* **2002**, *58*(1), 73–78. DOI 10.1016/S1386-1425(01)-00524-8.
- [31] L. Masgrau, A. González-Lafont, J. M. Lluch, Mechanism of the Gas-Phase HO + H₂O → H₂O + OH Reaction and Several Associated Isotope Exchange Reactions: A Canonical Variational Transition State Theory Plus Multidimensional Tunneling Calculation, *J. Phys. Chem. A* **1999**, *103*(8), 1044–1053. DOI 10.1021/jp983749t.
- [32] Th. Koops, T. Visser, W. M. A. Smit, Measurement and interpretation of the absolute infrared intensities of NH₃ and ND₃, *J. Mol. Struct.* **1983**, *96*(3), 203–218. DOI 10.1016/0022-2860(83)-90049-2.
- [33] V. A. Job, S. B. Kartha, V. B. Kartha, K. B. Thakur, Rotational analysis of the ν₂ band of NH₂D, *J. Mol. Spectrosc.* **1986**, *120*(1), 205–218. DOI 10.1016/0022-2852(86)90082-2.
- [34] V. A. Job, S. B. Kartha, K. Singh, V. B. Kartha, Inversion-rotation interaction in NH₂D: Intensity perturbations in the ν₂ band, *J. Mol. Spectrosc.* **1987**, *126*(2), 290–306. DOI 10.1016/0022-2852(87)90238-4.
- [35] L. Coudert, A. Valentin, L. Henry, Inversion doubling in the ν₂ vibration-rotation band of NH₂D and ND₂H, *J. Mol. Spectrosc.* **1986**, *120*(1), 185–204. DOI 10.1016/0022-2852(86)90081-0.
- [36] M. Snels, H. Hollenstein, M. Quack, The NH and ND stretching fundamentals of 14NH₂D, *J. Mol. Spectrosc.* **2006**, *237*(2), 143–148. DOI 10.1016/j.jms.2006.03.006.
- [37] E. Canè, L. Fusina, G. D. Lonardo, F. Tamassia, M. Villa, Infrared spectroscopy of 14ND₃: Analysis of the ν₂/ν₄/2ν₂ and ν₁/ν₃/2ν₄ band systems, *HITRAN2016 Spec. Issue* **2017**, *203*, 398–409. DOI 10.1016/j.jqsrt.2017.03.028.
- [38] H. C. Allen, E. D. Tidwell, E. K. Plyler, Infrared Spectra of Hydrogen Cyanide and Deuterium Cyanide, *J. Chem. Phys.* **1956**, *25*(2), 302–307. DOI 10.1063/1.1742876.
- [39] M. E. Jacox, D. E. Milligan, Low-Temperature Infrared Study of Intermediates in the Photolysis of HNCO and DNCO, *J. Chem. Phys.* **1964**, *40*(9), 2457–2460. DOI 10.1063/1.1725546.
- [40] V. K. Wang, J. Overend, High-resolution spectra of the ν₂ and 2ν₂ bands of HCN and DCN, *Spectrochim. Acta Part Mol. Spectrosc.* **1973**, *29*(4), 687–705. DOI 10.1016/0584-8539(73)80099-6.
- [41] P. F. Bartunek, E. F. Barker, The Infrared Absorption Spectra of the Linear Molecules Carbonyl Sulphide and Deuterium Cyanide, *Phys. Rev.* **1935**, *48*(6), 516–521. DOI 10.1103/PhysRev.48.516.
- [42] R. A. Ashby, R. L. Werner, The infra-red absorption spectrum of DNCO, *Spectrochim. Acta* **1966**, *22*(7), 1345–1353. DOI 10.1016/0371-1951(66)80038-3.
- [43] V. E. Bondybey, J. H. English, C. W. Mathews, R. J. Contolini, Infrared spectra and isomerization of CHNO species in rare gas matrices, *J. Mol. Spectrosc.* **1982**, *92*(2), 431–442. DOI 10.1016/0022-2852(82)90113-8.
- [44] E. Catalano, C. E. Rolon, A study of the thermal decomposition of confined triaminotrinitrobenzene. The gaseous products and kinetics of evolution, *Thermochim. Acta* **1983**, *61*(1), 37–51. DOI 10.1016/0040-6031(83)80302-5.
- [45] E. D. Loughran, E. M. Wewerka, R. N. Rogers and J. K. Berlin, The Influence of Metals on the Thermal Decomposition of Triaminotrinitrobenzene (TATB), Proceedings of the International Symposium on Analytical Methods for Propellants and Explosives, Karlsruhe, Germany, June 22–24, 1977, Las Alamos National Laboratory Report LA-UR-77-857.
- [46] B. J. Yancey, N. K. Muetterties, E. M. Kahl, E. A. Glascoe and J. G. Reynolds, Evolved Gas Analysis of the Thermal Decomposition of TATB and TATB-Based Plastic Bonded Explosives from the Small to Large Scales, International Detonation Symposium, Cambridge, MD, 2018.
- [47] K. Coffee, J. A. Olivas, A. F. Panasci, B. J. Stewart, E. M. Kahl, and J. G. Reynolds, Analysis of Thermally Damaged LX-17—Methods Development, Lawrence Livermore National Laboratory Report CODT-2021-0138, January 25, 2021.
- [48] A. K. Burnham, R. K. Weese, Kinetics of thermal degradation of explosive binders Viton A, Estane, and Kel-F, *Thermochim. Acta* **2005**, *426*(1), 85–92. DOI 10.1016/j.tca.2004.07.009.
- [49] A. K. Burnham, V. L. Stanford, S. Vyazovkin, E. M. Kahl, Effect of Pressure on TATB and LX-17 Thermal Decomposition, *Thermochim. Acta* **2021**, 178908. DOI 10.1016/j.tca.2021.178908.
- [50] S. Özkar, R. G. Finke, Silver Nanoparticles Synthesized by Microwave Heating: A Kinetic and Mechanistic Re-Analysis and Re-Interpretation, *J. Phys. Chem. C* **2017**, *121*(49), 27643–27654. DOI 10.1021/acs.jpcc.7b06323.
- [51] L. Bentea, M. A. Watzky, R. G. Finke, Sigmoidal Nucleation and Growth Curves Across Nature Fit by the Finke–Watzky Model of Slow Continuous Nucleation and Autocatalytic Growth: Explicit Formulas for the Lag and Growth Times Plus Other Key Insights, *J. Phys. Chem. C* **2017**, *121*(9), 5302–5312. DOI 10.1021/acs.jpcc.6b12021.
- [52] E. M. Kahl, N. K. Muetterties, A. J. Nelson, H. E. Mason, J. V. Crowhurst, K. R. Coffee, J. S. Moore, J. G. Reynolds, Characterization of Solid Residue Formation in LX-17 Exposed to Abnormal Thermal Environments, *AIP Conference Proceedings* **2020**, *2272*, 050010. DOI: 10.1063/12.0000948.
- [53] J. A. Carter, J. M. Zaug, A. J. Nelson, M. R. Armstrong, and M. R. Manaa, Ultrafast Shock Compression and Shock-Induced Decomposition of 1,3,5-Triamino-2,4,6-trinitrobenzene Subjected to a Subnanosecond-Duration Shock: An Analysis of Decomposition Products, *J. Phys. Chem. A* **2012**, *116*(20), 4851–4859. DOI 10.1021/jp301771y.
- [54] D. Quan, E. Herbst, Y. Osamura, E. Roueff, Gas-grain modeling of isocyanic acid (HNCO), cyanic acid (HOCN), fulminic acid (HCNO), and isofulminic acid (HONC) in assorted interstellar environments, *Astrophys. J.* **2010**, *725*(2), 2101–2109. DOI 10.1088/0004-637x/725/2/2101.

Manuscript received: March 21, 2021

Revised manuscript received: May 15, 2021

Version of record online: June 8, 2021